PNAS RESEARCH ARTICLE | ENGINEERING
BIOPHYSICS AND COMPUTATIONAL BIOLOGY OPEN ACCESS

Virtual ultrasound machine operating in a GHz to MHz frequency range for particle-based biomedical simulations

Urban Čoko[a,b], Tilen Potisk[a,b], and Matej Praprotnik[a,b,c,1]

Edited by Steve Granick, University of Massachusetts at Amherst, Amherst, MA; received March 24, 2026; accepted June 18, 2026

Ultrasound–matter interactions underpin numerous biomedical and soft-matter applications, yet simulating these phenomena is challenging due to the large separation of viscous and sonic time scales. Continuum methods capture large-scale wave propagation but cannot resolve microscale interactions, while particle-based approaches offer molecular resolution but struggle with efficiency and stability at larger scales. We introduce a particle-based virtual ultrasound machine that uses a smoothed dissipative particle dynamics variant with an implicit pressure solver and a negative-pressure stabilization scheme, required to mimic acoustic propagation across medically relevant MHz–GHz frequencies. We demonstrate its capabilities by modeling the acoustophoresis of encapsulated microbubbles, a key mechanism in ultrasound-mediated drug delivery. Beyond this application, the approach establishes a generalizable platform for simulating wave–matter interactions in soft and biological materials, opening promising directions for computational studies of acoustics-driven phenomena in science and engineering.

ultrasound | compressibility | smoothed dissipative particle dynamics | acoustophoresis | particle-based simulations

Significance

Particle-based simulations of ultrasound at mesoscopic scales are essential for understanding how acoustic waves interact with microbubbles, cells, and other soft biological structures, but existing methods struggle to achieve numerical stability, realistic fluid properties, and computational efficiency in the medically relevant MHz–GHz regime. We address this challenge by introducing usSDPD, a particle-based ultrasound simulation method combining an implicit compressible pressure solver with negative-pressure stabilization to allow for stable, efficient, and physically consistent acoustic wave propagation at submicron resolution. Based on usSDPD, we develop a virtual ultrasound machine that enables predictive in silico modeling of ultrasound for biomedical applications.

In modern medicine, ultrasound (US) has become an indispensable modality, used both for imaging and therapeutic purposes. For imaging applications, its most advantageous features are the absence of ionizing radiation and relatively low purchase and maintenance costs (1). It is applied extensively in soft-tissue imaging—from fetal monitoring to echocardiography (1)—and in therapeutic settings, where focused US enables tumor ablation and low-intensity US promotes tissue healing (2).

The frequency ranges of medical US vary with application. Therapeutic US generally uses lower frequencies (typically 0.5 to 3 MHz) (3). Diagnostic US typically operates between 2 MHz and 40 MHz (4), with lower frequencies (1 to 5 MHz) providing greater penetration depth (e.g. abdominal or cardiac scans), and higher frequencies (20 to 40 MHz) offering better spatial resolution for superficial structures (e.g. skin or small animal imaging) (1, 4). For instance, at 15 to 20 MHz, the imaging depth is about 3 to 4 cm, whereas at 50 MHz it decreases to 9 mm (1, 5). Acoustic excitations in the 100 MHz–GHz range are largely limited to research applications. GHz US can probe subcellular and molecular-scale motions; for example, GHz acoustic pulses have been shown to stimulate neuronal ion channels (6). Moreover, protein vibrational modes often lie in the GHz–THz range, with some low-frequency modes strongly correlated with large-amplitude conformational changes triggered by ligand binding (7–9).

For diagnostic imaging, contrast agents must exhibit resonance within the diagnostic frequency range. Among the most widely used agents are encapsulated microbubbles (EMBs)—gas-filled spheres encapsulated by lipid or protein shells, typically a few micrometers in diameter (10, 11). When exposed to US, EMBs undergo oscillations that produce strong, distinctive acoustic signals, enabling clear contrast between blood flow and surrounding tissues (5, 11, 12). Beyond imaging, EMBs can serve as vehicles for targeted drug delivery: Under sufficiently high acoustic pressures, their shells rupture through cavitation, inducing localized mechanical stress that temporarily increases cell membrane permeability—a process known as sonoporation (10). This phenomenon facilitates site-specific delivery of therapeutic agents, reducing systemic dosage and minimizing side effects. Furthermore, EMBs can be functionalized with ligands that bind to disease-specific biomarkers, allowing them to accumulate selectively at pathological sites such as tumor vasculature (10).

Conducting experimental studies in this domain is far from trivial. The parameters of EMBs are typically constrained to those achievable in laboratory conditions, and generating US itself requires specialized equipment. Therapeutic US systems generally operate at a single frequency or a limited set of discrete frequencies and deliver average

Author affiliations: [a]Theory Department, National Institute of Chemistry, Ljubljana SI-1001, Slovenia; [b]Department of Physics, Faculty of Mathematics and Physics, University of Ljubljana, Ljubljana SI-1000, Slovenia; and [c]Universitat de Barcelona Institute of Complex Systems, Barcelona 08028, Spain

Author contributions: U.Č., T.P., and M.P. designed research; U.Č. performed research; U.Č. analyzed data; and U.Č., T.P., and M.P. wrote the paper.

The authors declare no competing interest.

This article is a PNAS Direct Submission.

[1]To whom correspondence may be addressed. Email: praprot@cmm.ki.si.

This article contains supporting information online at https://www.pnas.org/lookup/suppl/doi:10.1073/pnas.2610567123/-/DCSupplemental.

Published July 16, 2026.

intensities up to 3 W/cm^2 (13). While intensity can be adjusted either discretely or continuously, the range of accessible intensities in practice remains narrow. Consequently, exploring a broad parameter space experimentally is challenging. To overcome these limitations, numerical simulations are frequently employed as a preliminary platform for investigation, effectively serving as a virtual laboratory before physical experiments are performed.

Designing a virtual US machine requires a fluid model that accurately captures both the viscosity and the acoustic properties of water at micrometer scale. This is difficult in practice because, as the system size increases, viscous and acoustic timescales become increasingly separated, rendering the problem multiscale (Section 2.1). Traditionally, such scenarios have been tackled using hybrid frameworks—such as PROTEUS (14)—that employ distinct solvers for sound propagation and fluid dynamics, coupling them through interactions with immersed structures. Common approaches for acoustic wave modeling include k-Wave (15), Field II (16), and SIMUS (17–19), while fluid flow is typically handled using continuum, mesh-based methods such as the lattice-Boltzmann method (LBM) and various computational fluid dynamics (CFD) techniques. In some cases, numerical methods are coupled with analytical solutions to reduce computational demands (20). While hybrid approaches are useful for certain special use-cases, their implementation is highly complex, system-dependent, and employs numerous simplifications.

On the other hand, particle-based fluid descriptions offer a compelling alternative to mesh-based methods, especially for biophysical simulations. Most notably, they are inherently compatible with particle-based models of immersed structures, since both are Lagrangian in nature. In contrast, coupling Lagrangian particle-based structures with Eulerian mesh-based fluids often necessitates complex interpolation schemes, such as Peskin's Immersed Boundary Method (21), which can compromise both model accuracy and simplicity. Furthermore, mesh-based methods generally struggle to resolve fine structural details unless the grid spacing is significantly smaller than the features of interest or adaptive meshing is employed. Particle-based methods also often provide a straightforward implementation of multiphase systems and thermal fluctuations, which are more challenging to implement in mesh-based formulations. Finally, dense suspensions are typically represented with higher fidelity in particle-based simulations, further underscoring their suitability for complex biophysical environments. Interestingly, particle-based US simulations and experimental approaches exhibit fundamentally opposing challenges. In experimental settings, achieving lower frequencies in the MHz range is relatively straightforward, whereas generating THz frequencies poses significant problems. In contrast, particle-based simulations readily reach THz frequencies but encounter difficulties at MHz frequencies, where numerical freezing artifacts typically arise (22).

In this paper, we design a particle-based virtual US machine capable of simulating US propagation at the micrometer scale (MHz frequencies), thereby enabling more versatile in silico experimentation. We achieve this by developing a method termed usSDPD that is based on smoothed dissipative particle dynamics (SDPD). usSDPD is a particle-based method that can faithfully capture both the viscosity and the speed of sound of water at micrometer scales, while also minimizing elastic artifacts that typically appear under highly negative pressures. This method makes it possible to study synthetic and biological systems previously inaccessible to particle-based approaches (Fig. 1). It enables the modeling of dense suspensions of immersed structures and their interactions without introducing excessive technical complexity. The virtual US machine presented here is envisioned as a core component of a general virtual US framework. This framework will integrate the virtual US machine with detailed models of immersed structures, such as EMBs and gas vesicles (26), enabling comprehensive simulations of US interactions with complex biological and synthetic systems. Together, these elements will provide a versatile platform for exploring US-based imaging, therapy, and mechanistic studies entirely in silico.

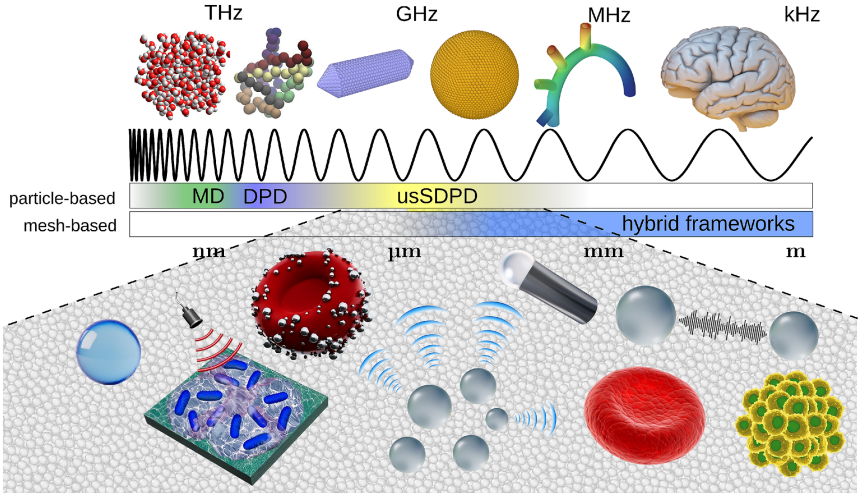

Fig. 1. Overview of spatiotemporal scales, simulation methods, and systems, studied with US. *Top*: commonly used methods for US simulations and the length- and frequency-scales they typically describe. Boundaries between methods are approximate, as the applicable range depends on computational resources, geometry, and optimizations. Representative systems are shown below the frequencies: molecular dynamics (MD) for all-atom simulations of water, dissipative particle dynamics (DPD) for THz excitations in proteins, and hybrid frameworks for large-scale biological tissue simulations (such as capillary flow) and EMB dynamics. Our method, usSDPD, fits on the medically relevant scale of EMBs. This figure shows the ranges, where the viscosity and compressibility match those of water. For example, the DPD method might be used also at larger scales, but either the compressibility and viscosity of water would not be correct, or a liquid with lower compressibility and/or higher viscosity would be used. *Bottom*: schematic representations of structures that can be coupled with usSDPD, including (from *Left* to *Right*) hydrogel microspheres, biofilms (23), red blood cell microrobots with magnetic nanoparticles (24), scattering EMBs, tubular microrobots (25), red blood cells, interacting oscillating EMBs, tumor spheroids, and others.

1. Results and Discussion

We present a particle-based fluid simulation method, termed usSDPD, that enables accurate modeling of US wave propagation in weakly compressible fluids such as water. On this basis, we construct a virtual US machine to simulate a sample immersed in water and positioned between two opposing US transducers. The virtual US machine is applied to simulate EMB acoustophoresis, demonstrating its ability to capture US-driven particle dynamics and illustrating its potential as a versatile tool for investigating a broad range of US-mediated phenomena.

1.1. Fluid Simulation. We assess the usSDPD method by characterizing its stability, viscosity, and pressure behavior at granularities of 0.01 μm, 0.1 μm, and 1 μm, where granularity denotes the fluid particle diameter. Appropriate timescales for each granularity are provided in *SI Appendix*, section A, along with detailed analyses and parameter tables *SI Appendix*, sections B and C. Our results indicate that a granularity of 1 μm and higher is not sufficiently accurate for our intended application. At 0.1 μm granularity, our method exhibits a substantial gain in numerical stability compared to SDPD, enabling a 40-fold increase in the maximum stable timestep, while inducing only a minor rise in viscosity. In contrast, simulations at 0.01 μm do not exhibit comparable improvements in timestep length, and further refinement to even smaller granularities is not advantageous, as DPD-based methods are inherently more suitable at nanoscopic scales. Consequently, usSDPD is best applied at granularities of 0.01 μm and 0.1 μm, with the greatest benefits observed at 0.1 μm granularity.

Next, we demonstrate that although the SDPD formulation exhibits significant deficiencies when applied to the virtual US machine, the proposed usSDPD approach remains robust. To assess its performance, we simulate a fluid block enclosed by periodic boundary conditions (PBCs) in all directions, where the simulation cell volume is periodically oscillated to generate bulk pressure oscillations. These volumetric oscillations induce corresponding variations in pressure and density, enabling direct assessment of the method's response to large-amplitude acoustic forcing. As shown in Fig. 2, the SDPD formulation becomes unstable at negative pressures, whereas the usSDPD method remains stable over a broad range spanning both positive and negative pressures throughout the entire oscillatory cycle. This indicates that the usSDPD method can successfully sustain strong periodic compressions and rarefactions without breakdown.

1.2. Virtual Ultrasound Machine. A particle-based virtual US machine consists of two key components: a particle-based fluid simulation method capable of reproducing fluid compressibility at the target length scale, and a mechanism for imposing pressure oscillations at the boundaries of the simulation domain, representing a simplified model of a US transducer. For the fluid dynamics at mesoscopic granularities (0.01 μm, 0.1 μm) and low-compressibility fluids such as water (MHz to GHz frequencies), we employ the previously introduced usSDPD method. At nanoscopic length scales (THz frequencies), however, DPD has been shown to be more appropriate; this is discussed in detail in *SI Appendix*, section B, and such virtual US machines may therefore employ DPD as a fluid simulation method. The virtual US machine considered here is realized by placing two transducers on opposing sides of the simulation box, which confines both the fluid and the immersed structure in one direction, while enforcing PBCs at the remaining two spatial directions. The transducers are modeled using the open boundary molecular dynamics (OBMD) method (Section 2.4) for simulating an open system of particles (27) (Fig. 3). In addition to generating pressure oscillations, OBMD enables the application of controlled shear stresses, a capability not available in conventional US transducers and particularly useful for investigating shear-driven flows.

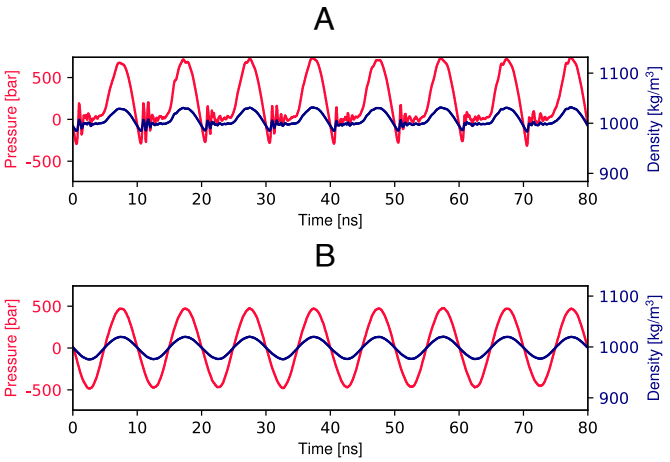

Fig. 2. Response of (*A*) standard (vanilla) SDPD and (*B*) usSDPD fluids to bulk volume oscillation. Both simulations are done at 0.1 μm granularity with both speed of sound and viscosity matched to those of water. usSDPD shows more stable behavior than vanilla SDPD at negative pressures. The pressure amplitude is large compared to the density amplitude, which is characteristic of water with low compressibility. In vanilla SDPD simulations, 10 times smaller timestep is used for stability.

1.3. Acoustophoresis Simulation. Our virtual US machine is designed to simulate US–fluid–structure interactions in weakly compressible fluids, such as water from nanometer to micrometer granularities. As a representative application, we study the dynamics of an EMB in a standing US field, where its motion is driven by acoustic radiation forces. These forces originate from the mismatch in compressibility and density between the EMB and the surrounding fluid and give rise to acoustophoresis, i.e., migration of the EMB within the acoustic field (28). In a standing wave, acoustic radiation forces drive the migration of immersed structures toward either pressure nodes or pressure antinodes, the latter typical for EMBs and the former typical for immersed beads. Acoustophoresis enables precise acoustic manipulation and is widely used in microfluidics for particle sorting, purification (29), concentration (30), washing (31), enrichment (32), and confinement trapping (33). It is also the driving mechanism behind acoustic tweezers (34). Analytical models (28, 35–37) and numerical simulations (38, 39), including finite element methods (40), have long been employed to study these forces.

The model of the experimental system includes the external fluid, the EMB membrane, and the internal fluid within the EMB, see Fig. 4. For the external fluid we employ the usSDPD method, which allows pressure waves of large amplitude to

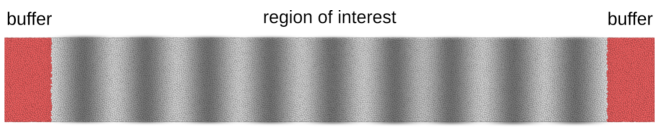

Fig. 3. Schematic of a virtual US machine. The machine consists of two US sources positioned at the left and right boundaries of the open simulation box (buffers), as well as the region of interest, where the immersed structure is located. By imposing oscillations of the same frequency in the left and right buffers, a standing wave field is generated in the region of interest (dark and light regions correspond to low and high density, respectively).

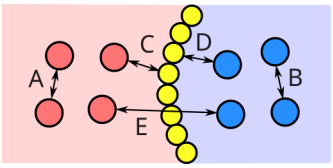

Fig. 4. Interactions in the acoustophoresis simulation system. Red circles represent external fluid particles, yellow circles represent membrane particles, and blue circles represent internal fluid particles. The arrows denote interactions between particle types.

be simulated without introducing excessive spurious elasticity, Section 1.1. The membrane is described using an isotropic elastic model (26, 41), which places membrane particles in the vertices of the triangulated EMB surface, and calculates forces by taking derivatives of the total elastic energy with respect to vertex positions. Because the membrane thickness is well below the fluid resolution scale, membrane-scale stress transfer is not explicitly resolved but treated through effective interactions between the fluid and the membrane. For the range of ultrasound pressure amplitudes and frequencies considered in this work, this approximation is sufficient to capture the microbubble dynamics. At higher pressure amplitudes, where the shell undergoes larger deformations, increased spatial resolution may be necessary to accurately resolve the fluid–structure interactions. For a detailed list of parameters, see *SI Appendix*, section C. Most notably, in our setup, the EMB is modeled as neutrally buoyant to allow for a larger timestep. However, its internal fluid remains significantly more compressible than water. Because of this high compressibility, we adopt the standard DPD method rather than SDPD for modeling the internal fluid. This reduces both the computational overhead and the number of parameters in the simulation. Moreover, it highlights the modularity of the particle-based framework, wherein distinct fluid models can be seamlessly coupled. In contrast, integrating a particle-based EMB model with a mesh-based fluid solver would require the use of interpolation techniques, such as Peskin's Immersed Boundary Method (21), to mediate interactions across the particle–mesh interface. Such approaches introduce additional algorithmic complexity and may compromise numerical accuracy. The final component of the model involves specifying the interactions between different types of particles. We assume an impermeable EMB membrane. For interactions between the external fluid and the membrane, we use the Akinci boundary condition (42), commonly employed in smoothed particle hydrodynamics (SPH) for incompressible and weakly compressible fluids. This boundary condition has the important property that the boundary force is invariant with respect to the sampling density (resolution) of the boundary, which is crucial for an oscillating EMB whose sampling density changes dynamically. It should also be noted that Monaghan's artificial pressure lowers the pressure only for nonboundary fluid particles; Akinci boundary particles still experience the full pressure force. Because ordinary DPD differs fundamentally from SDPD, the same boundary condition cannot be applied to interactions between the internal fluid and membrane particles. In this case, we employ a simple Lennard-Jones (LJ) interaction (Fig. 4).

Finally, we apply this modeling framework to simulate acoustophoresis in a standing wave for an open system of length 2.4 μm (Fig. 5). The standing wave is generated by enforcing in-phase harmonic oscillations in the buffer regions. Simulations are performed at five uniformly spaced viscosities ranging from $\eta = 1.0 \times 10^{-4}$ Pa s to $\eta = 8.9 \times 10^{-4}$ Pa s. In all cases, the EMB tends toward the pressure antinode; however, the characteristic migration time is shorter at lower viscosities. According to the theoretical model presented in ref. 43, the time required for a compressible particle to traverse a given distance scales linearly with viscosity—a trend we also observe in the simulation (Fig. 5). In these simulations, fewer than four iterations of the implicit-compressible pressure solver are typically required, indicating rapid pressure convergence. In general, the number of required iterations increases with increasing positive or negative pressures, but empirically we find it to remain below ten for all practical cases. Total system momentum is conserved in the simulation, which means that the external fluid acquires a net velocity as the EMB moves toward the pressure antinode. In order to suppress the global drift and focus on the relative motion of the EMB with respect to the standing-wave field, we enforce zero net momentum of the external fluid by subtracting its COM velocity at each timestep. This procedure constrains the bulk fluid to remain at rest, modeling a laboratory-frame description in which the recoil of the fluid is effectively suppressed by a much larger reservoir. Because the standing-wave field establishes on timescales much shorter than those associated with fluid drift, the acoustic forces are expected to be unaffected by the drift correction.

To demonstrate the scalability of our method, we perform a larger simulation at a frequency of 39 MHz, which falls within the medical US regime (4), see Fig. 6. In this case, the simulation cell length is increased to 10 μm, the width to 1.2 μm, and the EMB diameter to 0.6 μm. The pressure amplitude is gradually ramped up to its final value over the first 0.15 μs. We observe that the EMB consistently settles at the pressure antinode. To investigate the dynamics, we compare EMB trajectories under five different pressure amplitudes. The COM motion of the EMB transitions from an oscillatory pattern at short times (when EMB velocity is high) toward a constant value at longer times (when EMB velocity is low), see *Insets* in Fig. 6*C*. This behavior is consistent with the Bjerknes-force-based interpretation of EMB dynamics (44): away from pressure antinodes, the instantaneous pressure gradient oscillates, producing an effective oscillating buoyancy that drives COM displacement. At the pressure antinode, the instantaneous gradient vanishes, eliminating buoyancy and thus halting COM motion. According to ref. 43, the time required for a compressible particle to traverse a given distance scales as Δp^{-2}, where Δp is the pressure amplitude. This scaling agrees with our simulations (Fig. 6*E*).

2. Methods

An integral component of our virtual US machine is a particle-based fluid simulation method. Such a method must satisfy several key requirements: It should remain numerically stable over short and long simulation times, be thermodynamically consistent, and accurately reproduce the fundamental hydrodynamic properties of the target fluid, in particular its viscosity and speed of sound, which are essential for the correct description of acoustic wave propagation. The method should also be coarse-grained (CG) to avoid the high costs of an all-atom simulation. CG particle-based fluid simulation methods represent multiple fluid molecules with a single CG particle, where the number of molecules per particle–known as the mapping number, N_m–characterizes the level of coarse-graining. Methods such as Martini, DPD, and many-body DPD (MDPD) are commonly used for mesoscale fluid simulations (45). However, as the mapping number increases, these approaches face significant challenges, including numerical freezing and instabilities. Specifically, in DPD water, crystallization occurs once the mapping number approaches 20–provided that correct physical viscosity and compressibility are enforced simultaneously (22, 46). This freezing is linked to the Kirkwood–Alder transition (47), observed as mapping number and speed of sound increase. The root cause is entropy loss: Coarse-graining removes internal degrees of freedom, shifting free-energy

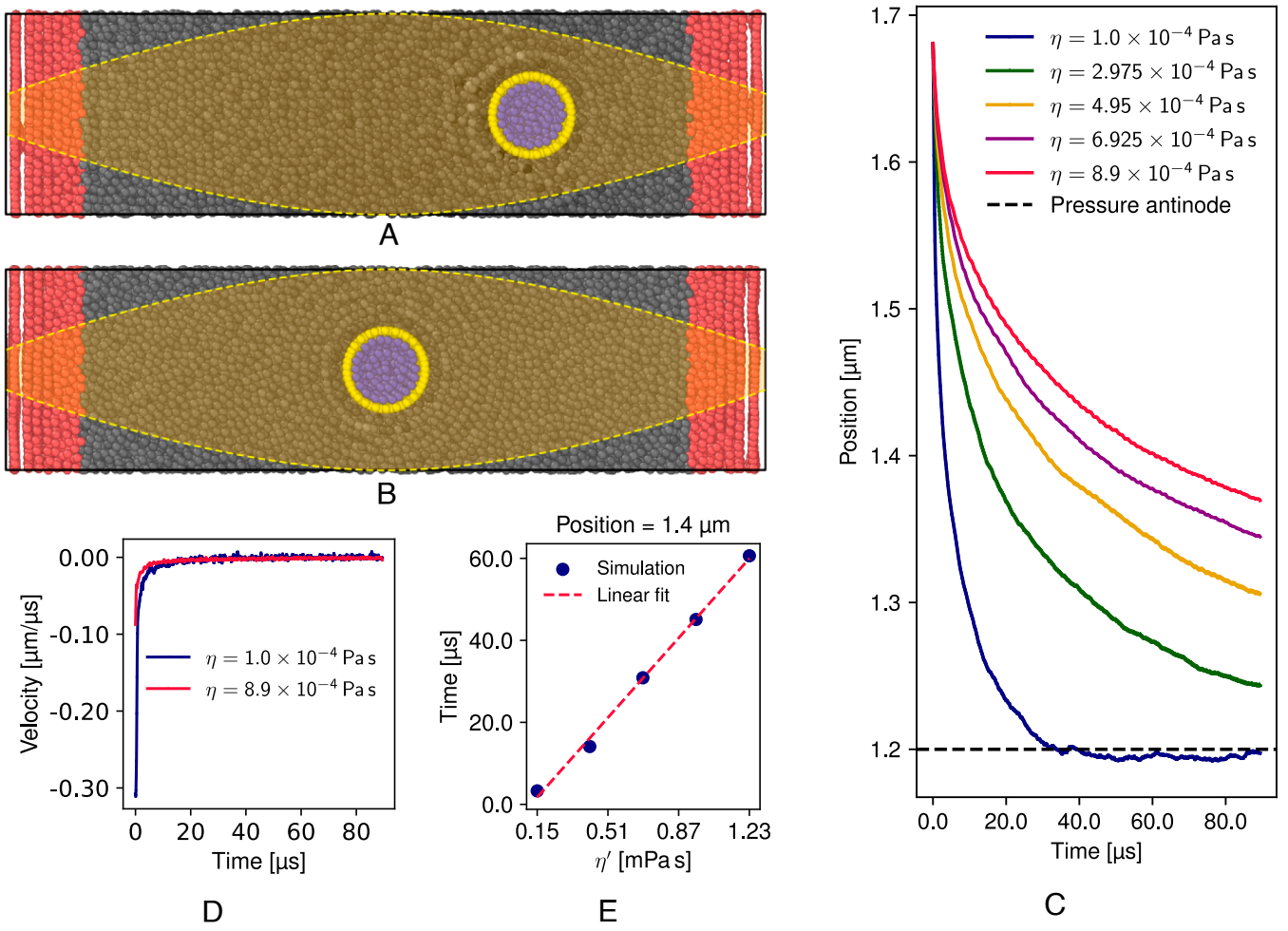

Fig. 5. Acoustophoresis simulation in a 2.4 μm × 0.63 μm × 0.63 μm cell. The US frequency is 178.4 MHz and the EMB diameter is 0.24 μm. (*A*) Snapshot at the beginning and (*B*) the end of the simulation (the simulation system is sliced in half along the page plane to increase visibility). Buffer regions are shown in red and the yellow dashed line schematically represents the standing wave field. (*C*) Trajectories of the EMB center-of-mass (COM) for viscosities $\eta = 1.0 \times 10^{-4}$Pa s *to* 8.9×10^{-4}Pa s at pressure amplitude $\Delta p = 9$ bar. (*D*) EMB COM velocities for the smallest and largest viscosity. (*E*) Time for the EMB to reach $x = 1.4$ μm as a function of simulated viscosity η'.

minima so that the system may exhibit a premature phase transition to a frozen state even at conditions where the original atomistic system is liquid (48, 49).

Another well-known model for CG particle-based simulations is Martini 3 (50), which typically represents four water molecules with a single particle. Martini 3 water consists of particles that interact via pairwise LJ interactions, tuned to reproduce the properties of water. This model is also plagued by freezing artifacts (45), which necessitate the use of so-called "antifreeze particles" (51). At the nanoscale, alternative methods such as DPD and MDPD have been shown to better reproduce the properties of water required for US simulations (45).

MDPD allows higher CG levels while maintaining the correct compressibility. However, stability requirements force a reduction of the timestep, which negates most of the computational advantages at CG levels beyond $N_m = 10^3$ (in our simulations, we achieve $N_m = 10^6$) (22, 52). Thus, achieving sufficiently high CG levels for US simulations requires a different approach.

Yet another particle-based method commonly used in fluid mechanics simulations is smoothed particle hydrodynamics (SPH) (53). This method differs substantially from DPD-based methods in that it is derived as a discretization of the Navier–Stokes equations (a top–down approach), unlike the DPD method, which is neither a top–down or bottom–up method (54). Continuum hydrodynamics has been shown to persist down to surprisingly small scales, enabling the application of continuum theory even at the mesoscale (55). At such scales, however, molecular discreteness becomes significant, as particles exhibit thermal motion that is negligible in macroscopic systems. SPH does not account for thermal fluctuations, which restricts its applicability to macroscopic and upper-mesoscale systems. To address this limitation, SPH has been modified to include thermal fluctuations consistent with the first and second laws of thermodynamics, introducing the method known as smoothed dissipative particle dynamics (SDPD) (56). This approach later became widely adopted for particle-based simulations at the mesoscopic scale. In its original form, however, SDPD is not suitable for simulations of US propagation at the mesoscopic scale due to the "tensile instability" artifact, which causes the fluid to fracture prematurely under tensile stress. In the following sections, we introduce the extended version of SDPD, coined usSDPD, designed to address the tensile instability artifact in the simulations of US propagation in weakly compressible fluids.

The simulations are performed using LAMMPS (57). While SDPD is already implemented in LAMMPS, we extended it by adding an implicit compressible pressure solver and packaged it into the package `ICSDPD`. Additional modifications to overcome tensile instability can be optionally enabled or disabled in the code.

2.1. Smoothed Dissipative Particle Dynamics (SDPD). SDPD is a particle-based method for simulating hydrodynamics, combining elements of SPH and DPD (56, 58). The main advantage of SDPD over SPH is that it incorporates thermal fluctuations in a manner consistent with the first and second laws of thermodynamics. Compared to DPD, SDPD offers several additional benefits. It allows a general equation of state (EOS) to be specified as input, rather than being limited to the fixed quadratic EOS used in DPD. Moreover, physical parameters such as viscosity and speed of sound can be specified directly, rather than being inferred empirically from non-physical DPD parameters. Finally, mapping the system to a physical scale is straightforward, in contrast to DPD.

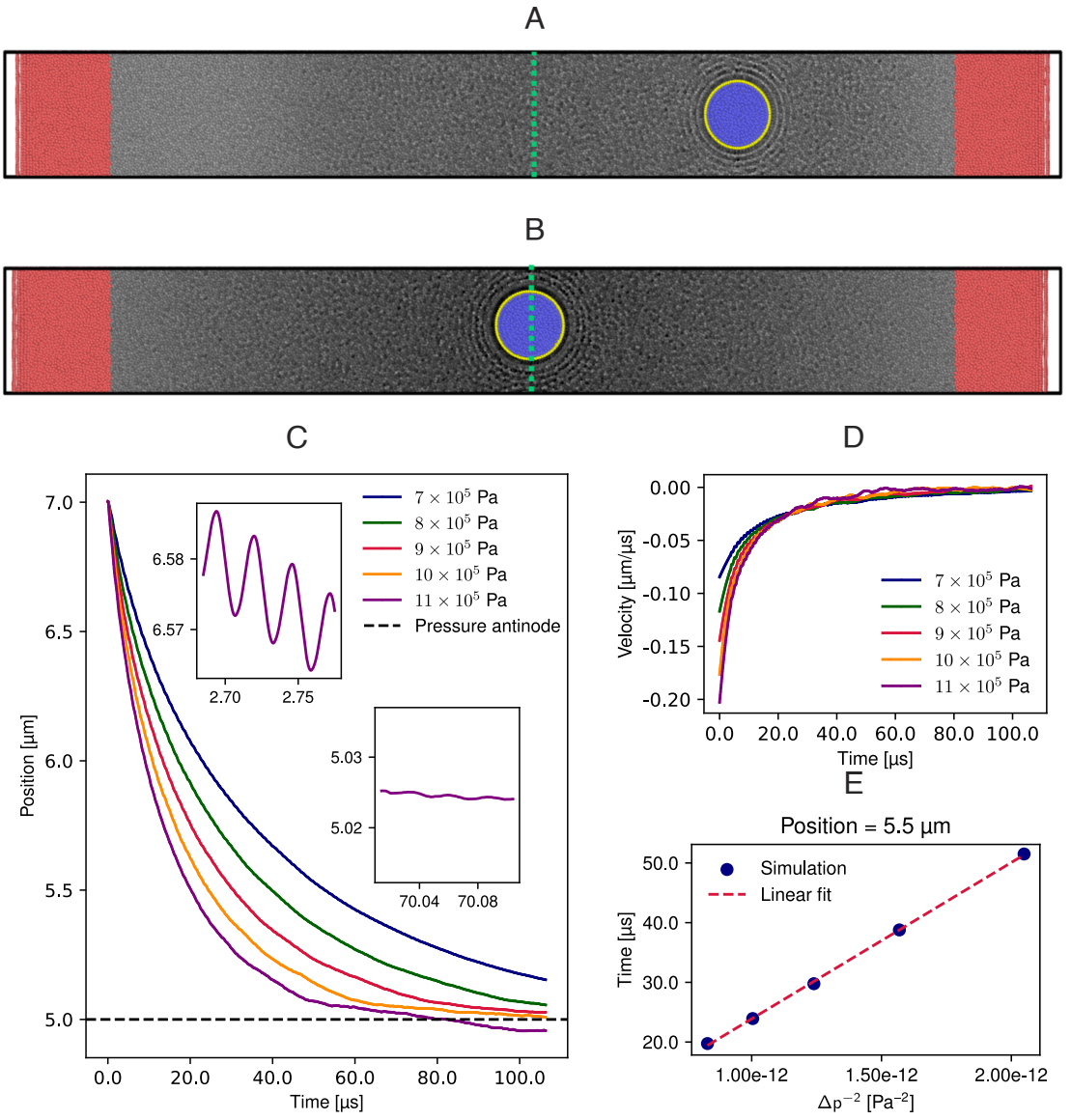

Fig. 6. Acoustophoresis simulations in a 10 μm × 1.2 μm × 1.2 μm cell. The US frequency is 38.6 MHz and the EMB diameter is 0.6 μm. (*A*) snapshot of the acoustophoresis simulation at the beginning and (*B*) the end of the simulation (the simulation system is sliced in half along the page plane to increase visibility). Buffer regions are shown in red and the green dashed line denotes the pressure antinode. (*C*) Trajectories of the EMB COM with input viscosity $\eta = 1.0 \times 10^{-4}$ Pa s. Each colored curve corresponds to a different pressure amplitude listed in the legend. *Insets* show a zoomed-in part of the trajectory with the highest pressure amplitude at two different times. (*D*) EMB COM velocity, corresponding to the position plot in (*C*). (*E*) Time required for an EMB to reach the position $x = 5.5$ μm as a function of the inverse square of the pressure amplitude.

For an isothermal fluid, the governing equations read:

$$\begin{aligned}
\frac{\mathrm{d}\mathbf{r}_i}{\mathrm{d}t} &= \mathbf{v}_i \\
\frac{\mathrm{d}\rho_i}{\mathrm{d}t} &= -\sum_j m_j \mathbf{v}_{ij} \cdot w'_{ij} \hat{\mathbf{e}}_{ij} \\
m_i \frac{\mathrm{d}\mathbf{v}_i}{\mathrm{d}t} &= \frac{5\eta}{3} \sum_j \frac{m_i m_j}{\rho_i \rho_j} \frac{w'_{ij}}{r_{ij}} \left(\mathbf{v}_{ij} + \hat{\mathbf{e}}_{ij} \hat{\mathbf{e}}_{ij} \cdot \mathbf{v}_{ij} \right) \\
&\quad - \sum_j m_i m_j \left(\frac{p_i}{\rho_i^2} + \frac{p_j}{\rho_j^2} \right) w'_{ij} \hat{\mathbf{e}}_{ij} \\
&\quad + \sum_j \sqrt{\frac{20\eta}{3} k_B T \frac{m_i m_j}{\rho_i \rho_j} w'_{ij}} \frac{\mathrm{d}\overline{\mathrm{W}}_{ij}}{\mathrm{d}t} \cdot \hat{\mathbf{e}}_{ij},
\end{aligned} \qquad [1]$$

where $\mathbf{r}_i$, $\mathbf{v}_i$, m_i, ρ_i, and p_i denote the position, velocity, mass, density, and pressure of the i-th particle, respectively. $\hat{\mathbf{e}}_{ij} = \mathbf{r}_{ij}/r_{ij}$ is the unit vector along $\mathbf{r}_{ij} \equiv \mathbf{r}_i - \mathbf{r}_j$, $\mathbf{v}_{ij} \equiv \mathbf{v}_i - \mathbf{v}_j$, and w'_{ij} is the magnitude of the kernel function gradient, such that $\nabla_i W_{ij} = w'_{ij} \hat{\mathbf{e}}_{ij}$, with $W_{ij} \equiv W(\mathbf{r}_i - \mathbf{r}_j)$. In all simulations, we use the cubic spline kernel and neglect the bulk viscosity. $\mathrm{d}\overline{\mathrm{W}}_i$ is the symmetric part of a 3 × 3 matrix of independent Wiener process increments. The independent Wiener process increments can be simulated as $\zeta(\Delta t)^{1/2}$, where ζ is an independent Gaussian random number and Δt is the timestep. Further details are provided in refs. 56 and 59.

SDPD and SPH are structurally closely related, differing primarily in that SDPD incorporates thermal fluctuations. Consequently, numerical strategies developed for SPH can be readily extended to SDPD. With this in mind, we employ the standard (leapfrog) SPH integrator for all SDPD implementations in this paper. The procedure is available in the SPH package of LAMMPS and is summarized in *Algorithm* 1. In addition, we compute particle densities using the commonly adopted summation form of the continuity equation,

$$\rho_i = \sum_j m_j W_{ij}. \quad [2]$$

as this formulation simplifies the implementation of boundary conditions (see code for details).

Algorithm 1 Smoothed particle hydrodynamics time integration scheme

procedure PRE-FORCE COMPUTATIONS
  for all particles i **do**
    compute half-step velocity: $\mathbf{v}_i^{t+\Delta t/2} = \mathbf{v}_i^t + \frac{\Delta t}{2m_i}\mathbf{f}_i^t$
    compute predicted velocity: $\tilde{\mathbf{v}}_i^{t+\Delta t} = \mathbf{v}_i^t + \frac{\Delta t}{m_i}\mathbf{f}_i^t$
    compute position: $\mathbf{r}_i^{t+\Delta t} = \mathbf{r}_i^t + \Delta t\, \mathbf{v}_i^{t+\Delta t/2}$
procedure FORCE COMPUTATION
  for all particles i **do**
    compute new forces $\mathbf{f}_i^{t+\Delta t}$
procedure POST-FORCE COMPUTATIONS
  for all particles i **do**
    compute full-step velocity: $\mathbf{v}_i^{t+\Delta t} = \mathbf{v}_i^{t+\Delta t/2} + \frac{\Delta t}{2m_i}\mathbf{f}_i^{t+\Delta t}$

In SDPD, scaling length and time by 10 reduces dimensionless temperature by 1,000 and dimensionless viscosity by 10, with speed of sound unchanged (*SI Appendix*, section A). An important consequence is that, at larger scales, the gap between the dimensionless speed of sound and the dimensionless viscosity widens, ultimately limiting the ability to simulate water at very high coarse-graining levels. This limitation is illustrated in *SI Appendix*, section B and has also been mentioned in ref. 45. A numerical value that quantifies the discrepancy between viscous and sonic time scales is the so-called compressibility factor (the ratio of the time for sound to travel one particle radius a to the time for viscous diffusion over the same distance) (60)

$$\varepsilon \equiv \frac{a/c}{a^2/\nu} = \frac{\nu}{ac}. \quad [3]$$

Moreover, the reduction of dimensionless temperature by a factor of 1,000 with each 10-fold increase in scale implies that thermal fluctuations rapidly become negligible compared to other forces when transitioning from the nanometer to the micrometer scale. For most simulations above the micrometer scale, thermal fluctuations should therefore be disabled. In the absence of thermal fluctuations, SDPD reduces to the well-known SPH method, commonly employed for macroscopic particle-based hydrodynamic simulations.

2.2. Implicit-Compressible Pressure Solver. There are some crucial differences in how DPD, SPH, and SDPD handle pressure computation. In DPD, the local pressure is not stored as a particle attribute but can be evaluated from particle positions, velocities, and forces using the Irving–Kirkwood formulation (61). In contrast, SPH and SDPD treat density and pressure as particle attributes. The particle density is computed through kernel interpolation, Eq. **2**, and is used to compute the pressure through an explicit EOS. For weakly compressible fluids, a common choice of EOS is

$$p_i = \rho_0 c^2 \left(\frac{\rho_i}{\rho_0} - 1\right), \quad [4]$$

where ρ_0 is the prescribed input density, c is the speed of sound, and ρ_i is the density of the i-th fluid particle. In weakly compressible fluids, the speed of sound greatly exceeds typical advective velocities, causing such explicit pressure computation to impose severe timestep constraints. To alleviate this limitation, we evaluate pressure forces using an implicit scheme, while dissipative and random forces are still treated explicitly (62–66). This hybrid approach permits timesteps up to 40 times larger than those of the original SDPD method (*SI Appendix*, section B).

An implicit pressure solver for compressible flows was originally developed within the SPH framework for snow simulations (66) and later incorporated into the open-source SPH solver SPlisHSPlasH (67). Given the structural similarity between SPH and SDPD, this pressure solver can be readily adapted to the SDPD framework. To derive the implicit compressible pressure solver, we begin from the continuity and Navier–Stokes equations,

$$\frac{D\rho}{Dt} + \rho\nabla\cdot\mathbf{v} = 0$$
$$\rho\frac{D\mathbf{v}}{Dt} = -\nabla p + \rho\mathbf{a}^{\text{non-pressure}},$$

where $\mathbf{a}^{\text{non-pressure}}$ includes all non-pressure forces acting on the fluid. After discretizing the equations, doing some simplifications and assuming a linear EOS, we get (62–64, 66)

$$-c^{-2}p^{t+\Delta t} + \Delta t^2\nabla^2 p^{t+\Delta t} = \rho_0^t - \rho^*, \quad [5]$$

where c is the speed of sound, $\rho^* = \rho^t - \Delta t\rho^t\nabla\cdot\mathbf{v}^*$ and $\mathbf{v}^* = \mathbf{v}^t + \Delta t\mathbf{a}^{\text{non-pressure}}$. Here, ρ^t and $\mathbf{v}^t$ are the density and velocity at timestep t, and $\mathbf{a}^{\text{non-pressure}}$ denotes the contribution to the fluid particle acceleration from dissipative and random forces. $V_i = m_i/\rho_i$ is the volume of the i-th particle. The summations in the algorithm are performed over fluid particles (indexed by j), boundary particles (indexed by b), or both (indexed by k). The implicit compressible pressure solver employs the relaxed Jacobi iteration to solve Eq. **5** iteratively; iteration step is denoted with the superscript (ℓ). *Algorithm* 2 provides a slightly modified version of the procedure described in ref. 66. In the algorithm, $\psi = 1.5$, and $\omega = 0.5$. A graphical overview of the timestepping procedure is shown in Fig. 7. The implicit compressible pressure solver iterates until the density error falls below 0.1 %, i.e. when $\frac{1}{N}\sum_i \left(\rho_0 - \rho_i^* - (A p)_i^{(\ell)}\right) < 0.001\rho_0$, where N is the total number of fluid particles.

2.3. Providing Stability at Negative Pressures (usSDPD). In SPH, SDPD, and related particle-based methods, pressure forces originate from the pressure term in the equations of motion. Around zero pressure, these forces are minimal, but their magnitude increases with both positive and negative pressures. In an equilibrium fluid, large pressure forces acting on individual particles largely cancel, resulting in a relatively small net force. However, any inherent instabilities in the method become strongly pronounced at high positive or negative pressures. The extent of compression or expansion at which instabilities inhibit simulations depends on the rate at which pressure changes with density, i.e., the speed of sound. This explains why the same methods perform better in fluids with higher compressibility (lower speed of sound) than in those with lower compressibility (higher speed of sound). One such instability is tensile instability, which manifests as premature fluid fracture under negative pressures. This instability poses a significant challenge for simulating US propagation, as acoustic waves involve alternating regions of high and low pressure; in the low-pressure regions, tensile instability can emerge and disrupt the simulation. We observe that many existing remedies for tensile instability make the fluid slightly viscoplastic (introduce some spurious elasticity) at highly positive/negative pressures (68–71). While such modifications may be acceptable for certain systems, they are unsuitable for studies of acoustic radiation forces, as in the present work. These artifacts become particularly pronounced at larger scales–where thermal fluctuations are negligible–and in low Mach number flows, where convective time scales are much slower than acoustic time scales. In some cases, these spurious elastic forces can even lead to freezing phenomena at high positive or negative pressures.

It can be shown, following Swegle (72), that tensile instability arises when $W''T > 0$, where W'' is the second derivative of the kernel with respect to its argument, and T is the tensile stress (positive for tension and negative for compression). From this condition, it follows that a region stable under tension is unstable under compression, and vice versa. The condition is illustrated in Fig. 8.

To mitigate instabilities at high negative pressures, we introduce two additional modifications. First, we reduce the fluid particle diameter from 0.5 h to 0.3 h, where h is the kernel cutoff. As a result, the typical number of neighbors increases from approximately 60 to about 250, slightly raising

Algorithm 2 Solver steps of the implicit compressible pressure solver.

procedure PREPARE
  for all particles i **do**
    compute $\mathbf{v}_i^* = \mathbf{v}_i^t + \Delta t \mathbf{a}_i^{\text{non-pressure}}$
    compute $\nabla \cdot \mathbf{v}_i^* = \sum_k (\mathbf{v}_k^* - \mathbf{v}_i^*) V_k \nabla W_{ik}$
    compute $\rho_i^* = \rho_i^t - \Delta t \rho_i^t \nabla \cdot \mathbf{v}_i^*$
    compute $a_{ii} = -c^{-2} - \Delta t^2 \sum_j V_i V_j \|\nabla W_{ij}\|^2 - \Delta t^2 \left(\sum_j V_j \nabla W_{ij} + \psi \sum_b V_b \nabla W_{ib} \right) \sum_k V_k \nabla W_{ik}$
procedure SOLVE
  while not converged **do**
    for all particles i **do**
      compute $\nabla p_i^{(\ell)} = \sum_j (p_j^{(\ell)} + p_i^{(\ell)}) V_j \nabla W_{ij} + \psi p_i^{(\ell)} \sum_b V_b \nabla W_{ib}$
    for all particles i **do**
      compute $\nabla^2 p_i^{(\ell)} = \sum_j (\nabla p_j^{(\ell)} - \nabla p_i^{(\ell)}) V_j \nabla W_{ij}$
      compute $(Ap)_i^{(\ell)} = -c^{-2} p_i^{(\ell)} + \Delta t^2 \nabla^2 p_i^{(\ell)}$
      compute $p_i^{(\ell+1)} = p_i^{(\ell)} + \frac{\omega}{a_{ii}} \left(\rho_0 - \rho_i^* - (Ap)_i^{(\ell)} \right)$
  In the SOLVE procedure, index $t + \Delta t$ is removed for clarity.

the computational cost. More importantly, some neighbor particles are then forced into the pair-instability regime, where particles form fully overlapping pairs with their neighbors (72). To avoid this issue, an additional LJ potential is introduced with a small, empirically determined well depth of $\varepsilon = 1 \times 10^{-21} J$ and $\sigma = 0.23\,h$, which is smaller than the particle diameter of $0.3\,h$. This potential has a minimum at $r_{ij} \approx 0.26\,h$. The purpose of this repulsion is to prevent pair instability when particles are unphysically close, while leaving the system unaffected when particles are reasonably separated. This means that at sustained positive pressures, fluid particles tend to cluster at some slightly smaller interparticle distance, determined by the LJ potential, however, the effect is weak and reversible, when pressures are lower. The idea of adding a LJ potential to the SPH method was first proposed by Monaghan (73), but was not implemented in that work. Although this approach is effective in our case, many potential improvements to the simple repulsive LJ potential remain possible. As demonstrated in *SI Appendix*, section B, the LJ potential introduces an additional viscosity contribution, which constrains the achievable coarse-graining level in our simulations. Improving the repulsive potential is left for future work.

The second modification incorporates Monaghan's "artificial pressure" to further improve stability at negative pressures (73). The main idea of artificial pressure is to reduce the magnitude of interparticle pressure forces under negative pressure, thereby shifting the onset of tensile instability toward lower pressures. To implement artificial pressure, we add an additional term Rf_{ij}^n to Eq. **1**, as follows

$$\left(\frac{p_i}{\rho_i^2} + \frac{p_j}{\rho_j^2} \right) \rightarrow \left(\frac{p_i}{\rho_i^2} + \frac{p_j}{\rho_j^2} + R f_{ij}^n \right), \qquad [6]$$

where $f_{ij} = W(r_{ij})/W(r_{\text{ave}})$ and r_{ave} is the average spacing between fluid particles (set to $0.3\,h$ in all simulations with artificial pressure). The factor R is computed using the procedure in [3], and n is set to 4. We note that under negative pressures, expression [**6**] simplifies to

$$\frac{p_i}{\rho_i^2} + \frac{p_j}{\rho_j^2} + R f_{ij}^n = \frac{p_i}{\rho_i^2} + \frac{p_j}{\rho_j^2} - \epsilon f_{ij}^n \left(\frac{p_i}{\rho_i^2} + \frac{p_j}{\rho_j^2} \right) \qquad [7]$$

$$= (1 - \epsilon f_{ij}^n) \left(\frac{p_i}{\rho_i^2} + \frac{p_j}{\rho_j^2} \right), \qquad [8]$$

which clearly illustrates the artificial reduction of pressure forces between fluid particles in the negative-pressure regime.

We further verify that usSDPD remains stable across a wide pressure range by examining the EOS, which is linear in our case (Eq. **4**). By definition, the pressure is zero when $\rho = \rho_0$. The speed of sound is obtained from the slope of the $p(\rho)$ curve using the standard relation $c^2 = \partial p / \partial \rho$, making EOS plots a direct means of verifying the speed of sound (compressibility) in the simulation. As shown in Fig. 9, both methods reproduce the expected linear EOS at densities above the reference density (positive pressures), and no upper stability limit was reached in our simulations. At densities below the reference density (negative pressures), however, the method without artificial pressure progressively deviates from the linear relation, whereas the usSDPD formulation with artificial pressure remains linear down to approximately -500 bar, substantially extending the stable negative-pressure regime. At very high tensions, we note that a small amount of spurious elasticity remains, but its magnitude is sufficiently low to be acceptable for our purposes.

2.4. Open Boundary Molecular Dynamics (OBMD). OBMD is a simulation framework designed to model nonequilibrium systems by enabling the controlled exchange of mass, momentum, and energy across the boundaries of a finite simulation domain (27). We use OBMD to model the transducers in the virtual US machine. The framework partitions the system into a central region of interest (ROI) and adjacent buffer zones, where particles are inserted

Algorithm 3 Computation of Artificial Pressure

procedure COMPUTEARTIFICIALPRESSURE
  $R_i = \max\left(-\frac{\epsilon p_i}{\rho_i^2}, 0 \right)$
  $R_j = \max\left(-\frac{\epsilon p_j}{\rho_j^2}, 0 \right)$
  if $p_i > 0$ **and** $p_j > 0$ **then**
    $R = 0.01 \left(\frac{p_i}{\rho_i^2} + \frac{p_j}{\rho_j^2} \right)$
  else
    $R = R_i + R_j$

ϵ is set to 0.3 in all simulations that use artificial pressure.

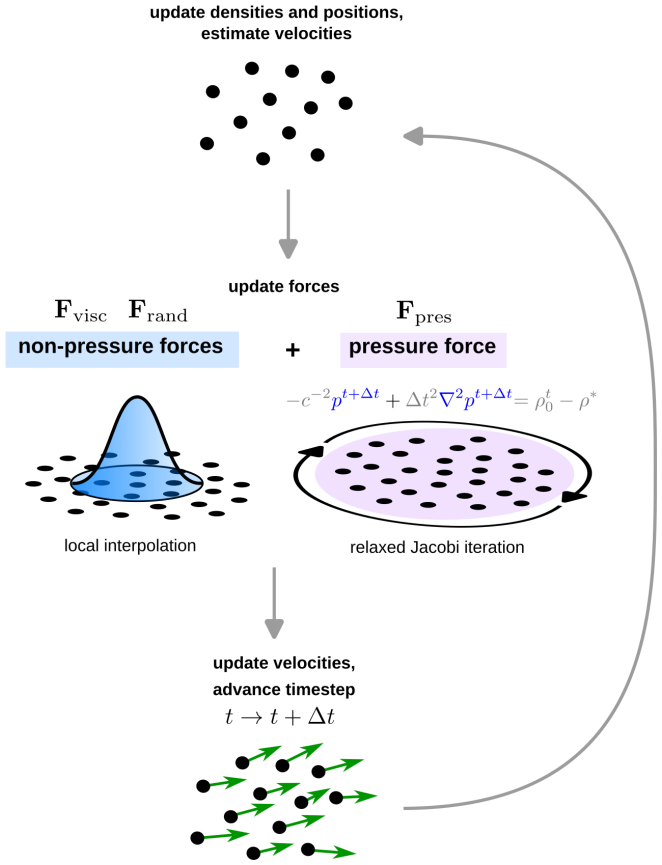

Fig. 7. Graphical representation of the timestepping procedure of the SDPD method with the implicit compressible pressure solver. For details, see *Algorithms* 1 and 2. First, the densities and positions of the particles are updated, and the velocities at the next timestep are estimated. These quantities are then used to update the forces. The so-called non-pressure forces (viscous and random contributions) are computed locally from particle properties. Subsequently, a global iteration procedure is carried out to compute the pressure for every particle, which is then used to determine the pressure force. Finally, the sum of the non-pressure and pressure forces is used to update the particle velocities and advance the timestep.

or removed. The particle number in each buffer is regulated by a feedback mechanism that ensures convergence toward a target density, while particle insertion is performed using energy-minimizing algorithms such as USHER (74). Boundary conditions are imposed by applying external forces to buffer particles, derived from a local momentum balance that accounts for both interparticle interactions and the momentum flux associated with particle exchange. This approach allows for the imposition of stress or velocity boundary conditions.

In order to correctly model the constant chemical potential of the system, the change in energy must be calculated when a particle is inserted at some position in the buffer. In simpler pairwise fluid methods, the energy increment is obtained by summing the additional pairwise contributions to the total energy for every neighbor of the inserted particle. In multibody, nonlocal methods such as the one used in this work, the exact calculation of the energy increment is more difficult, as the nonlocal effect of adding a particle on the pressure must be considered. Therefore, we employ a crude approximation, which is sufficient for the simple cases presented in this paper. To obtain the approximate energy increment, the density of the inserted particle is computed from the positions of its neighbors. The pressure of the inserted particle is then determined from its density using a simple Cole equation of state, instead of solving the pressure iteratively:

$$p_i = B\left[\left(\frac{\rho_i}{\rho_0}\right)^{\gamma} - 1\right], \qquad [9]$$

where $B = \rho_0 c^2/\gamma$, ρ_0 is the equilibrium density, c is the speed of sound, and $\gamma = 7$. The Cole equation is a standard choice for simulating water with SDPD, however, we could have as well chosen the linear EOS, since we use it in the implicit compressible pressure solver and the Cole EOS is approximately linear at the range of pressures we are working with. The approximate energy increment is then calculated as

$$\Delta E \approx p_i V_i - \frac{1}{2}\sum_j m_i m_j \left(\frac{p_i}{\rho_i^2} + \frac{p_j}{\rho_j^2}\right)\mathbf{v}_{ij}\cdot\nabla_j W_{ij}, \qquad [10]$$

where $V_i = m_i/\rho_i$. The first term on the right-hand side corresponds to the pressure work associated with creating a particle of volume V_i at pressure p_i, while the second term accounts for the energy increments from the SPH energy equation (equation 3.17 in ref. 53).

3. Conclusion

In this work, we developed a virtual US machine capable of simulating US–fluid–structure interaction between a weakly compressible fluid and immersed structures at mesoscopic (micrometer) scales, corresponding to medically relevant MHz–GHz frequency range. We achieved this by modifying the SDPD method to accurately reproduce acoustic wave propagation with realistic speed of sound and viscosity. By introducing an implicit compressible pressure solver, we extended the timestep by 40 times compared to explicit schemes—a significant improvement for weakly compressible fluids such as water. We also improved the EOS curves (eliminated tensile instability) by reducing the fluid particle diameter, introducing artificial pressure, and adding additional LJ interaction. This improved the stability of the US simulation at negative pressures, which is an essential part of any virtual US machine. Because the fluid simulation framework presented here is particle-based, it can be directly coupled with particle-based descriptions of immersed structures. As a proof of concept, we coupled the method with an elastic EMB filled with DPD particles and subjected it to US excitation. The coupled simulation successfully reproduced the expected migration of the EMB to the pressure antinode.

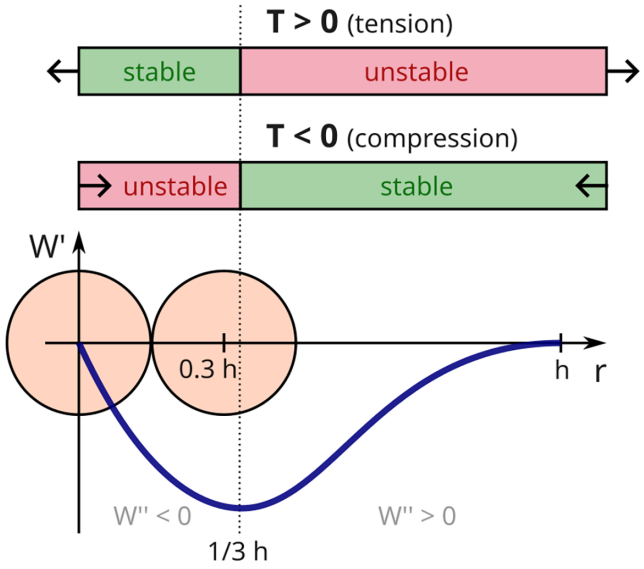

Fig. 8. Stable and unstable regimes of the SPH-based methods. First derivative of a cubic spline kernel (blue) along with regions of pair and tensile instabilities (red). The derivative of the cubic spline kernel has a minimum at $r = 1/3\,h$. Two particles are also shown to scale (orange) to illustrate that at zero background pressure, immediate neighbors are in the pair instability regime if $a = 0.3\,h$. For the conventional choice of $a = 0.5\,h$, immediate neighbors are in the tensile instability regime.

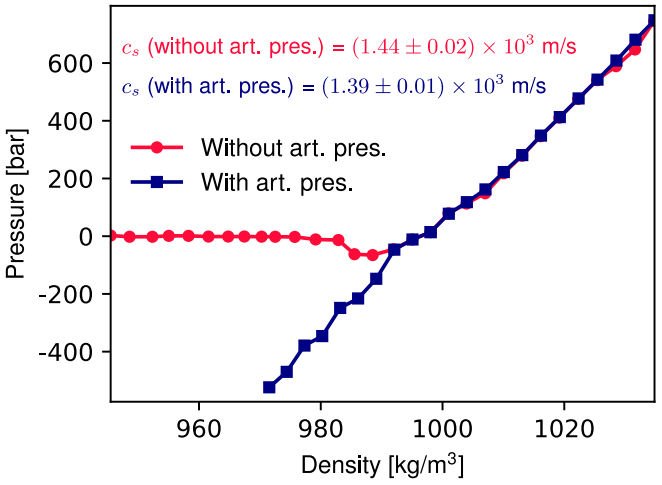

Fig. 9. Pressure–density relationship (EOS) for usSDPD with and without artificial pressure. Both simulations use a linear EOS. Without artificial pressure, the simulated EOS matches the input only at positive pressures; at negative pressures, a divergence caused by tensile instability becomes evident. In contrast, the method with artificial pressure accurately reproduces a linear EOS even under highly negative pressures. Simulations are performed on a 0.1 μm granularity with viscosity $\eta = 8.9 \times 10^{-4}$ Pa s and speed of sound $c_s = 1{,}481$ m/s at $T = 300$ K. Both pressure and density are measured using the nonbiased approach introduced in ref. 54. The *Inset* shows the speed of sound, obtained from the slope of the linear region of the EOS curve.

Some interesting research questions have been left for future investigation. For simplicity, the bulk viscosity of the surrounding fluid was set to zero, even though it strongly influences US attenuation. Consequently, the attenuation predicted by our simulations is not expected to match experimental observations. Since bulk viscosity is already included in the general SDPD framework, extending usSDPD to account for it is straightforward. Furthermore, the role of alternative interparticle repulsive interactions beyond the LJ potential remains unexplored; a more carefully designed repulsion may reduce viscosity artifacts while still preventing pair instability. Another direction for future work is the detailed investigation of fluid–membrane interactions, which were not addressed in this study. The method can, in principle, be extended to non-Newtonian fluids, such as blood, following approaches previously developed for SPH (75). In such formulations, viscosity is treated as a particle attribute that is dynamically updated from the local shear rate estimated using neighboring particles. Finally, realistic experimental conditions often involve traveling waves and arbitrary US pulse sequences rather than standing waves. This is particularly important for applications such as investigating the response of MB suspensions under pulsed US excitation, where short, high-intensity pulses are commonly used to minimize sample heating (76). Achieving this in simulation, however, requires the implementation of nonreflective boundary conditions (NRBCs) to prevent spurious wave reflections from the simulation boundaries. Several promising approaches for NRBCs have been proposed in related hydrodynamics and SPH contexts, including methods based on the method of characteristics (77), fluid-property extrapolation (78), and particle-property freezing (79). Although heating effects were not included in our isothermal formulation, the extension to a thermal US machine is feasible, since thermal effects are already incorporated in the most general SDPD method (56). The usSDPD method also presents certain limitations. At positive pressures, the method gradually develops pair instability, leading to particle clustering at the interaction range of the LJ potential. While negligible under oscillatory US conditions, this effect becomes relevant under sustained positive pressures. We speculate that adaptive kernels (53) could resolve this issue, which we leave for future work. At highly negative pressures, the method also exhibits some spurious elasticity.

In conclusion, the advances presented in this work establish a foundation for particle-based simulations of US propagation in mesoscopic systems. By combining improved numerical stability and natural coupling with particle-based structures, the virtual US machine provides a versatile framework for investigating US–fluid–structure interactions, with promising applications ranging from studies of wave propagation to studies of various mesoscale systems, such as gas vesicles, EMBs, red blood cells, microrobots, cells, and other biologically or technologically relevant structures.

Data, Materials, and Software Availability. Code data have been deposited in GitHub (https://github.com/L17-Projects/usSDPD) (80). All other data are included in the manuscript and/or *SI Appendix*.

ACKNOWLEDGMENTS. We acknowledge financial support under the ERC Advanced Grant MULTraSonicA (Grant No. 885155) from the European Research Council (ERC). We also acknowledge the European High Performance Computing Joint Undertaking (EuroHPC JU) for awarding the project ID EHPC-REG-2025R02-164 access to Vega at the Institute of Information Science (IZUM, Slovenia). We further thank dr. Franci Merzel for insightful discussions.

1. C. M. Moran, A. J. W. Thomson, Preclinical ultrasound imaging–A review of techniques and imaging applications. *Front. Phys.* **8**, 124 (2020).
2. T. M. Best, K. E. Wilk, C. T. Moorman, D. O. Draper, Low intensity ultrasound for promoting soft tissue healing: A systematic review of the literature and medical technology. *Intern. Med. Rev.* **2**, 271 (2016).
3. D. Miller *et al.*, Overview of therapeutic ultrasound applications and safety considerations. *J. Ultrasound Med. Off. J. Am Inst. Ultrasound Med.* **31**, 623–634 (2012).
4. D. Neumann, E. Kollorz, "Ultrasound" in *Medical Imaging Systems: An Introductory Guide*, A. Maier, S. Steidl, V. Christlein, J. Hornegger, Eds. (Springer, Cham (CH), 2018).
5. D. Maresca *et al.*, Biomolecular ultrasound and sonogenetics. *Annu. Rev. Chem. Biomol. Eng.* **9**, 229–252 (2018).
6. P. S. Balasubramanian, A. Singh, C. Xu, A. Lal, GHz ultrasonic chip-scale device induces ion channel stimulation in human neural cells. *Sci. Rep.* **10**, 3075 (2020).
7. F. Tama, Y. H. Sanejouand, Conformational change of proteins arising from normal mode calculations. *Protein Eng.* **14**, 1–6 (2001).
8. D. Tobi, I. Bahar, Structural changes involved in protein binding correlate with intrinsic motions of proteins in the unbound state. *Proc. Natl. Acad. Sci. U.S.A.* **102**, 18908–18913 (2005).
9. H. Wako, S. Endo, Ligand-induced conformational change of a protein reproduced by a linear combination of displacement vectors obtained from normal mode analysis. *Biophys. Chem.* **159**, 257–266 (2011).
10. J. A. Navarro-Becerra, M. A. Borden, Targeted microbubbles for drug, gene, and cell delivery in therapy and immunotherapy. *Pharmaceutics* **15**, 1625 (2023).
11. H. Yusefi, B. Helfield, Ultrasound contrast imaging: Fundamentals and emerging technology. *Front. Phys.* **10**, 791145 (2022).
12. B. Heiles, D. Terwiel, D. Maresca, The advent of biomolecular ultrasound imaging. *Neuroscience* **474**, 122–133 (2021).
13. G. ter Haar, Therapeutic ultrasound. *Eur. J. Ultrasound* **9**, 3–9 (1999).
14. B. Heiles *et al.*, PROTEUS: A physically realistic contrast-enhanced ultrasound simulator-Part II: Imaging applications. *IEEE Trans. Ultrason. Ferroelectr. Freq. Control.* **72**, 866–878 (2025).
15. B. E. Treeby, B. T. Cox, K-Wave: MATLAB toolbox for the simulation and reconstruction of photoacoustic wave fields. *J. Biomed. Optics* **15**, 021314–021314 (2010).
16. J. A. Jensen, Field: A program for simulating ultrasound systems. *Med. Biol. Eng. Comput.* **34**, 351–353 (1997).
17. D. Garcia, SIMUS: An open-source simulator for medical ultrasound imaging. Part I: Theory & examples. *Comput. Methods Programs Biomed.* **218**, 106726 (2022).
18. A. Cigier, F. Varray, D. Garcia, SIMUS: An open-source simulator for medical ultrasound imaging. Part II: Comparison with four simulators. *Comput. Methods Programs Biomed.* **220**, 106774 (2022).
19. D. Garcia, F. Varray, SIMUS3: An open-source simulator for 3-D ultrasound imaging. *Comput. Methods Programs Biomed.* **250**, 108169 (2024).
20. A. Pavlič, T. Baasch, Acoustic nanoparticle trapping is driven by synergy between acoustic and hydrodynamic interactions. *Phys. Rev. Lett.* **135**, 187201 (2025).
21. C. S. Peskin, The immersed boundary method. *Acta Numer.* **11**, 479–517 (2002).
22. S. Y. Trofimov, "Thermodynamic consistency in dissipative particle dynamics," PhD thesis, Technische Universiteit Eindhoven (2003).
23. J. Huang, Q. Fu, X. Shao, Y. Li, Ultrasonic strategies for mitigating microbial adhesion and biofilm formation on medical surfaces: A mini review. *Front. Microbiol.* **16**, 1558035 (2025).

24. D. Huang, L. Cai, N. Li, Y. Zhao, Ultrasound-trigged micro/nanorobots for biomedical applications. *Smart Med.* **2**, e20230003 (2023).
25. X. Lu *et al*., Ultrafast growth and locomotion of dandelion-like microswarms with tubular micromotors. *Small* **16**, 2003678 (2020).
26. N. Ntarakas, M. Lah, D. Svenšek, T. Potisk, M. Praprotnik, Dissipative particle dynamics models of encapsulated microbubbles and nanoscale gas vesicles for biomedical ultrasound simulations. *ACS Appl. Nano Mater.* **8**, 16053–16070 (2025).
27. R. Delgado-Buscalioni, J. Sablić, M. Praprotnik, Open boundary molecular dynamics. *Eur. Phys. J. Special Top.* **224**, 2331–2349 (2015).
28. L. P. Gor'kov, On the forces acting on a small particle in an acoustical field in an ideal fluid. *Sov. Phys. Doklady* **6**, 773 (1962).
29. C. W. Shields, C. D. Reyes, G. P. López, Microfluidic cell sorting: A review of the advances in the separation of cells from debulking to rare cell isolation. *Lab Chip* **15**, 1230–1249 (2015).
30. O. Jakobsson *et al*., Thousand-fold volumetric concentration of live cells with a recirculating acoustofluidic device. *Anal. Chem.* **87**, 8497–8502 (2015).
31. S. Deshmukh, Z. Brzozka, T. Laurell, P. Augustsson, Acoustic radiation forces at liquid interfaces impact the performance of acoustophoresis. *Lab Chip* **14**, 3394–3400 (2014).
32. C. Magnusson *et al*., Clinical scale cell-surface marker independent, acoustic microfluidic enrichment of tumor cells from blood. *Anal. Chem.* **89**, 11954–11961 (2017).
33. P. Ohlsson *et al*., Integrated acoustic separation, enrichment, and microchip polymerase chain reaction detection of bacteria from blood for rapid sepsis diagnostics. *Anal. Chem.* **88**, 9403–9411 (2016).
34. J. Shi *et al*., Acoustic tweezers: Patterning cells and microparticles using standing surface acoustic waves (SSAW). *Lab Chip* **9**, 2890–2895 (2009).
35. L. V. King, On the acoustic radiation pressure on spheres. *Proc. R. Soc. Lond. Ser. A Math. Phys. Sci.* **147**, 212–240 (1934).
36. K. Yosioka, Y. Kawasima, Acoustic radiation pressure on a compressible sphere. *Acta Acust. Acust.* **5**, 167–173 (1955).
37. I. Leibacher *et al*., Acoustophoresis of hollow and core-shell particles in two-dimensional resonance modes. *Microfluid. Nanofluid.* **16**, 513–524 (2014).
38. S. Sepehrirahnama, F. S. Chau, K. M. Lim, Numerical calculation of acoustic radiation forces acting on a sphere in a viscous fluid. *Phys. Rev. E* **92**, 063309 (2015).
39. D. Haydock, Lattice Boltzmann simulations of the time-averaged forces on a cylinder in a sound field. *J. Phys. A Math. Gen.* **38**, 3265–3277 (2005).
40. J. Wang, J. Dual, Numerical simulations for the time-averaged acoustic forces acting on rigid cylinders in ideal and viscous fluids. *J. Phys. A Math. Theor.* **42**, 285502 (2009).
41. M. Vlachomitrou, N. Pelekasis, Dynamic simulation of a coated microbubble in an unbounded flow: Response to a step change in pressure. *J. Fluid Mech.* **822**, 717–761 (2017).
42. N. Akinci, J. Cornelis, G. Akinci, M. Teschner, Coupling elastic solids with smoothed particle hydrodynamics fluids. *Comput. Animat. Virtual Worlds* **24**, 195–203 (2013).
43. H. Bruus, Acoustofluidics 7: The acoustic radiation force on small particles. *Lab Chip* **12**, 1014 (2012).
44. V. Bjerknes, *Fields of Force: A Course of Lectures in Mathematical Physics Delivered* (Columbia University Press, 1906), vol. 1.
45. M. Lah, N. Ntarakas, T. Potisk, P. Papež, M. Praprotnik, Open-boundary molecular dynamics of ultrasound using supramolecular water models. *J. Chem. Phys.* **162**, 024103 (2025).
46. I. V. Pivkin, G. E. Karniadakis, Coarse-graining limits in open and wall-bounded dissipative particle dynamics systems. *J. Chem. Phys.* **124**, 184101 (2006).
47. W. Dzwinel, D. A. Yuen, Matching macroscopic properties of binary fluid to the interactions of dissipative particle dynamics. *Int. J. Mod. Phys. C* **11**, 1–25 (2000).
48. V. P. Sokhan, M. A. Seaton, I. T. Todorov, Phase behaviour of coarse-grained fluids. *Soft Matter* **19**, 5824–5834 (2023).
49. K. M. Kidder, R. J. Szukalo, W. G. Noid, Energetic and entropic considerations for coarse-graining. *Eur. Phys. J. B* **94**, 153 (2021).
50. P. C. T. Souza *et al*., Martini 3: A general purpose force field for coarse-grained molecular dynamics. *Nat. Methods* **18**, 382–388 (2021).
51. S. J. Marrink, H. J. Risselada, S. Yefimov, D. P. Tieleman, A. H. De Vries, The MARTINI force field: Coarse grained model for biomolecular simulations. *J. Phys. Chem. B* **111**, 7812–7824 (2007).
52. I. Pagonabarraga, D. Frenkel, Dissipative particle dynamics for interacting systems. *J. Chem. Phys.* **115**, 5015–5026 (2001).
53. J. J. Monaghan, Smoothed particle hydrodynamics. *Annu. Rev. Astron. Astrophys.* **30**, 543–574 (1992).
54. P. M. Kulkarni, C. C. Fu, M. S. Shell, L. Gary Leal, Multiscale modeling with smoothed dissipative particle dynamics. *J. Chem. Phys.* **138**, 234105 (2013).
55. B. J. Alder, Decay of the velocity autocorrelation function. *Phys. Rev. A* **1**, 18–21 (1970).
56. P. Español, M. Revenga, Smoothed dissipative particle dynamics. *Phys. Rev. E* **67**, 026705 (2003).
57. A. P. Thompson *et al*., LAMMPS - a flexible simulation tool for particle-based materials modeling at the atomic, MESO, and continuum scales. *Comput. Phys. Commun.* **271**, 108171 (2022).
58. M. Ellero, P. Español, Everything you always wanted to know about SDPD★ (★ but were afraid to ask). *Appl. Math. Mech.* **39**, 103–124 (2018).
59. M. Jalalvand, M. A. Charsooghi, S. Mohammadinejad, Smoothed dissipative particle dynamics package for LAMMPS. *Comput. Phys. Commun.* **255**, 107261 (2020).
60. R. Tatsumi, R. Yamamoto, Propagation of hydrodynamic interactions between particles in a compressible fluid. *Phys. Fluids* **25**, 046101 (2013).
61. M. B. Liu, G. R. Liu, L. W. Zhou, J. Z. Chang, Dissipative particle dynamics (DPD): An overview and recent developments. *Arch. Comput. Methods Eng.* **22**, 529–556 (2015).
62. C. Hu, M. Kashiwagi, A CIP-based method for numerical simulations of violent free-surface flows. *J. Mar. Sci. Technol.* **9**, 143–157 (2004).
63. H. Ikari, H. Gotoh, T. Sakai, H. Tanioka, Analysis of impact wave pressure by particle method for compressible fluid. *Annu. J. Coast. Eng. JSCE* **52**, 731–735 (2005).
64. A. Khayyer, H. Gotoh, Modified moving particle semi-implicit methods for the prediction of 2D wave impact pressure. *Coast. Eng.* **56**, 419–440 (2009).
65. B. Solenthaler, R. Pajarola, Predictive-corrective incompressible SPH. ACM Trans. Graphics 28, Article No.: 40 (2009). https://doi.org/10.1145/1531326.1531346
66. C. Gissler, A. Henne, S. Band, A. Peer, M. Teschner, An implicit compressible SPH solver for snow simulation. *ACM Trans. Graph.* **39**, 36:1–36:16 (2020).
67. J. Bender *et al.*, SPlisHSPlasH_Library. GitHub. https://github.com/InteractiveComputerGraphics/SPlisHSPlasH. Accessed 12 August 2025.
68. H. Takeda, S. M. Miyama, M. Sekiya, Numerical simulation of viscous flow by smoothed particle hydrodynamics. *Prog. Theor. Phys.* **92**, 939–960 (1994).
69. P. W. Randles, L. D. Libersky, Normalized SPH with stress points. *Int. J. Numer. Methods Eng.* **48**, 1445–1462 (2000).
70. K. Sugiura, S. I. Inutsuka, An extension of Godunov SPH: Application to negative pressure media. *J. Comput. Phys.* **308**, 171–197 (2016).
71. L. D. G. Sigalotti, H. López, A. Donoso, E. Sira, J. Klapp, A shock-capturing SPH scheme based on adaptive kernel estimation. *J. Comput. Phys.* **212**, 124–149 (2006).
72. J. Swegle, D. Hicks, S. Attaway, Smoothed particle hydrodynamics stability analysis. *J. Comput. Phys.* **116**, 123–134 (1995).
73. J. Monaghan, SPH without a tensile instability. *J. Comput. Phys.* **159**, 290–311 (2000).
74. R. Delgado-Buscalioni, P. V. Coveney, USHER: An algorithm for particle insertion in dense fluids. *J. Chem. Phys.* **119**, 978–987 (2003).
75. N. S. Martys, W. L. George, B. W. Chun, D. Lootens, A smoothed particle hydrodynamics-based fluid model with a spatially dependent viscosity: Application to flow of a suspension with a non-Newtonian fluid matrix. *Rheol. Acta* **49**, 1059–1069 (2010).
76. M. Cheng, F. Li, T. Han, A. C. H. Yu, P. Qin, Effects of ultrasound pulse parameters on cavitation properties of flowing microbubbles under physiologically relevant conditions. *Ultrason. Sonochem.* **52**, 512–521 (2019).
77. M. Lastiwka, M. Basa, N. J. Quinlan, Permeable and non-reflecting boundary conditions in SPH. *Int. J. Numer. Methods Fluids* **61**, 709–724 (2009).
78. A. Tafuni, J. Domínguez, R. Vacondio, A. Crespo, A versatile algorithm for the treatment of open boundary conditions in Smoothed particle hydrodynamics GPU models. *Comput. Methods Appl. Mech. Eng.* **342**, 604–624 (2018).
79. J. M. M. Sh Khorasanizade, Sousa,, An innovative open boundary treatment for incompressible SPH. *Int. J. Numer. Methods Fluids* **80**, 161–180 (2016).
80. U. Čoko, T. Potisk, M. Praprotnik, usSDPD. GitHub. https://github.com/L17-Projects/usSDPD. Deposited 3 July 2026.